Research Article | Vol. 28, No. 10 / 11 May 2020 / Optics Express 14300
Optics EXPRESS

Early dynamics of cavitation bubbles generated during ns laser ablation of submerged targets

JIANGYOU LONG,[1,2,4] MATTHEW ELICEIRI,[2] ZACHARIAS VANGELATOS,[2] YOONSOO RHO,[2] LETIAN WANG,[2] ZHENGLIANG SU,[2] XIAOZHU XIE,[1,3] YONGKANG ZHANG,[1] AND COSTAS P. GRIGOROPOULOS[2,5]

[1]*Laser Micro/Nano Processing Lab, School of Electromechanical Engineering, Guangdong University of Technology, Guangzhou 510006, China*
[2]*Laser Thermal Laboratory, Department of Mechanical Engineering, University of California, Berkeley, California 94720-1740, USA*
[3]*State Key Laboratory of Precision Electronic Manufacturing Technology and Equipment, Guangdong University of Technology, Guangzhou 510006, China*
[4]*longjangpeter@gmail.com*
[5]*cgrigoro@berkeley.edu*

Abstract: In this study, we observe and study the early evolution of cavitation bubbles generated during pulsed laser ablation of titanium targets in different liquid environments utilizing a high-resolution stroboscopic shadowgraphy system. A hydrodynamic model is proposed to calculate the early pressure changes within the bubble and in the surrounding fluid. Our results show that the cavitation bubble is a low-pressure region that is bounded by a high-pressure fluid lamina after the incipient stage, and its evolution is primarily affected by the liquid density. Moreover, the initial bubble pressure increases substantially in high viscosity liquids. This work illuminates how the liquid properties affect the early bubble dynamics and is a step towards a deeper understanding of laser-materials interactions in liquid environments.

© 2020 Optical Society of America under the terms of the OSA Open Access Publishing Agreement

1. Introduction

Liquid-assisted laser processing has been studied in both industrial applications and in the context of nanoscience. In industrial applications, water has been chosen as a flexible confinement layer in laser shock peening [1], and a water-jet-guided laser machining technique has been widely utilized for fine cutting, drilling and grooving with a reduced heat-affected zone and mitigated debris, spatter, and recast [2,3]. In addition, pulsed laser ablation in liquid (PLAL) has been considered a simple, green, and versatile approach for the preparation of nanomaterials with various compositions (metals, alloys, oxides, etc.) and morphologies (nanoparticles, nanorods, nanotubes, etc.) without employing toxic chemicals [4,5].

When laser ablation occurs in air, the ejection of the ablated materials forms a plasma which expands rapidly in ambient air. However, due to the strong confinement of the liquid, an explosive cavitation bubble forms after the laser incidence and affects the subsequent process. Using in-situ small-angle X-ray scattering [6,7] and in-situ Rayleigh scattering [8], fast nucleation and growth of nanoparticles inside the cavitation bubbles have been observed. Furthermore, growth dynamics of laser-induced cavitation bubbles have been inquired via high-speed imaging [9,10], time-resolved shadowgraph imaging [11,12], time-resolved digital holograms [13], pump-probe microscope [14], and time-resolved photoelastic imaging [15]. These in-situ detection and imaging techniques promote our understanding and knowledge about laser ablation in liquid environments, but some critical mechanisms are still poorly understood. For example, even though the evolution of laser-induced cavitation bubbles in various liquids has been depicted

#391584 https://doi.org/10.1364/OE.391584
Journal © 2020 Received 27 Feb 2020; revised 22 Mar 2020; accepted 22 Mar 2020; published 27 Apr 2020

Optics EXPRESS

in lots of works, quantitative descriptions of the bubble pressure changes with time are still challenging.

In the study of cavitation-related phenomena, the basic description of the bubble dynamics is the nonlinear Rayleigh-Plesset (PR) equation, which expresses the changes of bubble pressure (P_B) with the bubble radius (R) [16]. In addition to the RP equation, considerations of the bubble contents are necessary. For simplicity, it is widely assumed that the bubble contains some quantity of non-condensable gas whose partial pressure is P_0 at some reference size R_0, and thus the gas pressure is determined by an adiabatic equation of state: $P_B = P_0(R_0/R)^{3\gamma}$, where γ is the heat capacity ratio [17,18]. As the laser-induced cavitation bubbles can grow up to several millimeters in diameter and last for several hundreds of microseconds, a low magnification imaging system and a long sampling interval, from hundreds of nanoseconds to several microseconds, were employed in most previous studies. Afterward, the changes of bubble radii with time were described by the RP equation combining with the adiabatic equation to depict the pressure changes within the bubble [9,10,19,20]. However, as the bubble contents were unknown, two critical parameters, P_0 and R_0, were generally assumed based on experience. The consequence is that quantitative descriptions of bubble pressure changes with time are difficult. For instance, the calculated initial bubble pressure after laser incidence differs greatly in different works, from 0.1 MPa to 10^4 MPa [9,10,19–21].

The present work aims to advance the understanding of laser ablation in liquid environments by providing a detailed experimental observation of the early evolution of cavitation bubbles generated during pulsed laser ablation of submerged titanium targets. Different from previous works, we focus on the evolution of laser-induced cavitation bubbles within 1 microsecond after the laser incidence. With high-resolution shadowgraph images, we provide a succinct depiction of the bubble dynamics during its critical stages when the bubble is miniscule, enabling a quantitative description of the bubble pressure changes with time.

2. Experimental setup

Figure 1 schematically depicts the experimental setup. A 1064 nm and a 532 nm Nd: YAG nanosecond (ns) laser are used for the ablation and imaging, respectively. After being expanded by a beam expander, the 1064 nm laser beam is reflected by a backside polished dichroic mirror and then focused by a 5X long working distance objective. The focused Gaussian laser spot, measured by the knife-edge method, is 48 μm in diameter. The focused laser beam then irradiates the polished titanium sample (Ti > 99.5 wt. %) with a thickness of 1 mm, which is positioned in a transparent container made by poly (methyl methacrylate) (PMMA) and is immersed at a depth of 5 mm below the liquid's surface. Deionized water and chemical pure ethanol, *n*-butanol and a poly(ethylene glycol) solution with an average molecular weight of 200 (PEG200) are used as the liquid. The 532 nm laser beam is initially focused by a convex lens and then enters a light pipe to form a laser spot with uniform energy distribution. The uniform laser spot is expanded by another convex lens to provide a large laser spot which can illuminate the whole container. The illuminating laser beam passes the surface of the Ti target, providing a shadowgraph image on a CCD camera (DCU223M from Thorlabs) coupled with a 12X zoom lens, a neutral-density (ND) filter, and a 2X long working distance objective. Both of the two laser beams are partly collected by two photodetectors (DET10A2 from Thorlabs) which are connected to an oscilloscope to measure their delay time (t) and their pulse widths. The measured pulse width (FWHM) of the 1064 nm and 532 nm laser is 20 ns and 4 ns, respectively. The delay time shown in the text is the time interval between two pulses' rising edge median (half-maximum). A delay generator (DG535 from Stanford) is employed to trigger the two laser beams at a designated delay time. Each acquisition triggers a single laser shot, allowing one photograph to be acquired at a given delay time. The sample is translated after each acquisition such that an unblemished region is used for each image. The obtained shadowgraph images are processed by a Sobel operator

Optics EXPRESS

to emphasize edges, and then the shockwaves and the cavitation bubbles are circularly fitted to measure their radius. A standard micrometer glass slide for microscope calibration with a minimum scale of 10 μm is used to determine the magnified pitch length of the images.

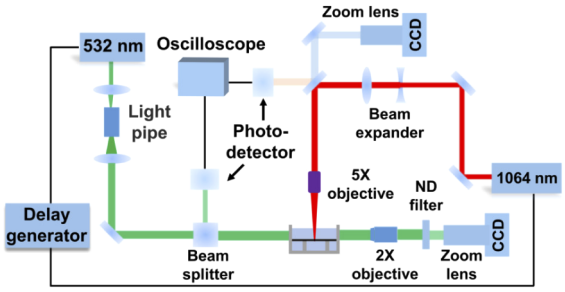

Fig. 1. Schematic of the experimental setup.

3. Results and discussion

Figure 2(a) and (b) convey the ns-resolved shadowgraph images in water after each laser incidence. Almost immediately after the laser incidence, a shadow area forms; and after less than 20 ns, the profiles of shockwaves (S) and cavitation bubbles (B) can be distinguished. Under low F [Fig. 2(a)], a hemispherical cavitation bubble can be observed after ~30 ns. Under high F [Fig. 2(b)], the nascent cavitation bubble has a conical shape and grows to a hemispherical shape after less than 100 ns. Penetration of some bubble contents into to the liquid is observed [t = 21 ns in Fig. 2(b)], which is probably caused by the violent ejection of laser-ablated materials. Similar phenomenon has been found previously when observing the initial evolution of laser-induced plasma and bubble simultaneously. When employing laser pulses with high peak power, the size of the nascent plasma is large than or similar to that of the nascent bubble [22].

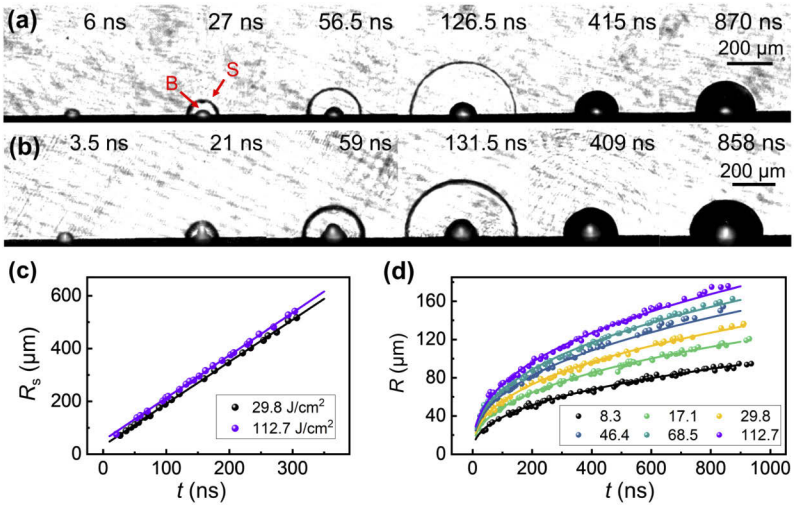

Fig. 2. (a, b) Shadowgraph images of shockwaves (S) and cavitation bubbles (B) generated after laser incidences. Laser fluence (F): (a) 29.8 J/cm^2 and (b) 112.7 J/cm^2. Inserted text: t. Liquid: deionized water. (c, d) Changes of shockwave radius (R_s) and cavitation bubble radius(R) with t in water. Solid lines in (c) and (d) are fitted curves by linear regression and Eq. (1), respectively. The legend in (d) shows the F with units of J/cm^2.

Optics EXPRESS

Figure 2(c) and (d) summarize the radii variation of the laser-induced shockwaves and cavitation bubbles in water. The experimental data points in Fig. 2(c) and (d) start from a $t \sim 20$ ns when the profiles of shockwaves and bubbles are discernible. During the initial 300 ns, as shown in Fig. 2(c), the generated shockwaves propagate at a nearly constant speed. When the F increases from 29.8 J/cm^2 to 112.7 J/cm^2, the average speed increases slightly from 1591 m/s to 1614 m/s. To put these values into perspective, the measured sound speed in water is 1497 m/s (at 25 °C) [23]. Moreover, the generation of shockwaves is also slightly quicker with increasing F. The velocity of emitted shockwaves is dependent on the absorbed laser energy. Previously, the average velocity of the emitted shockwave has been found to be 2600 m/s during the initial 200 ns when using 20 mJ laser pulses [12]. In comparison, the maximum pulse energy used in this work is only 1.02 mJ, which results in the low propagation speed of the shockwaves and the limited difference when changing the F.

Regarding to the cavitation bubbles, as shown in Fig. 2(d), we find that the early changes of bubble radius (R) with t (20 ns $< t <$ 900 ns) can be well fitted by a simple relationship:

$$R = at^{2/5}, \tag{1}$$

where a is a constant chiefly dependent on F. This simple expression enables analytic solutions of the pressure distribution within the bubble and in the surrounding liquid.

Assuming an incompressible liquid, the fluid velocity (u) at a radius of r ($r \geq R$) can be obtained via the continuity equation:

$$u(r) = \frac{R^2}{r^2}\frac{dR}{dt} = \frac{2}{5}\frac{a^3}{r^2}t^{1/5}. \tag{2}$$

For a Newtonian liquid, the Navier-Stokes equation used for motion in r direction can be written as:

$$-\frac{1}{\rho}\frac{\partial P}{\partial r} = \frac{\partial u}{\partial t} + u\frac{\partial u}{\partial r} - v[\frac{1}{r^2}\frac{\partial}{\partial r}(r^2\frac{\partial u}{\partial r}) - 2\frac{u}{r^2}], \tag{3}$$

where ρ, v and P is the liquid density, the kinematic viscosity and the fluid pressure, respectively. Applying Eq. (2) and Eq. (3), we get:

$$\begin{aligned} -\frac{1}{\rho}\frac{\partial P}{\partial r} &= \frac{2R}{r^2}\left(\frac{dR}{dt}\right)^2 + \frac{R^2}{r^2}\frac{d^2R}{dt^2} - \frac{2R^4}{r^5}\left(\frac{dR}{dt}\right)^2 \\ &= \frac{2}{25}\frac{a^3}{r^2}t^{-4/5} - \frac{8}{25}\frac{a^6}{r^5}t^{2/5}. \end{aligned} \tag{4}$$

Note that the viscous terms cancel during substitution. Integrating Eq.(4) from the bubble boundary $r = R$ to $r \to \infty$ gives:

$$\frac{P(R) - P_\infty}{\rho} = R\frac{d^2R}{dt^2} + \frac{3}{2}\left(\frac{dR}{dt}\right)^2 = 0. \tag{5}$$

Assuming that there is no mass transfer across the bubble boundary and the bubble content is homogenous, the boundary condition of the bubble can be written as [17]:

$$P(R) = P_B - \frac{4\mu}{R}\frac{dR}{dt} - \frac{2\sigma}{R}, \tag{6}$$

where μ and σ are the dynamic viscosity and surface tension, respectively; and P_B is the pressure within the bubble. Hence, we get a simplified Rayleigh-Plesset equation:

$$P_B = P_\infty + \frac{4\mu}{R}\frac{dR}{dt} + \frac{2\sigma}{R}. \tag{7}$$

Optics EXPRESS

The surrounding fluid pressure can also be obtained by integrating Eq. (4) from the bubble boundary $r = R$ to an arbitrary $r>R$:

$$\frac{P(r) - P(R)}{\rho} = \frac{2}{25}\frac{a^3 t^{-4/5}}{r}\left[1 - \frac{a^3 t^{6/5}}{r^3}\right]. \tag{8}$$

Therefore, we obtain that the pressure maximum ($P_{\max}$) in the surrounding fluid is achieved independently of the time at $r_{P\max}/R = 4^{1/3}$:

$$\frac{P_{\max} - P_\infty}{\rho} = \frac{3}{50}4^{-1/3}a^2 t^{-6/5}. \tag{9}$$

The constant a can be obtained based on the observed bubble evolution. Afterward, utilizing Eq. (7) - Eq. (9), we are able to calculate P_B, $P(r)$ and $P_{\max}$, respectively, which provide detailed descriptions of the pressure changes within the bubble and in the surrounding fluid. The results are presented in Fig. 3.

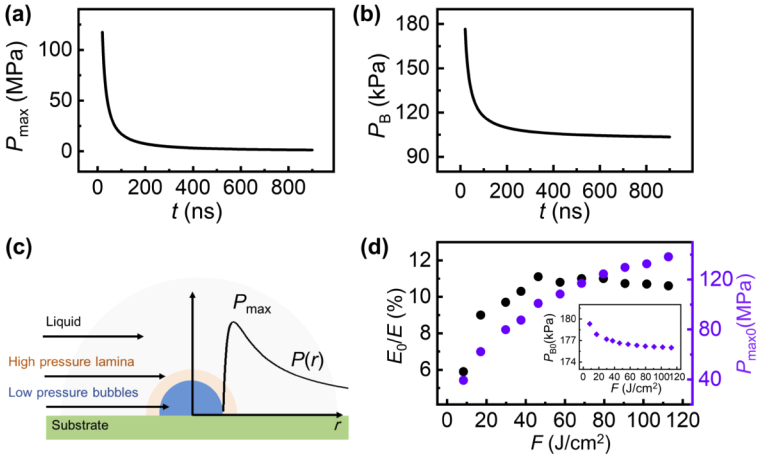

Fig. 3. (a, b) A typical evolution of the pressure maximum in the surrounding fluid ($P_{\max}$) and the pressure within the bubble (P_B) with t. F: 68.5 J/cm^2. (c) Schematic of a cavitation bubble and the surrounding liquid. Solid black curve: pressure distribution in the fluid $P(r)$. (d) Changes of E_0/E (black circles), $P_{\max 0}$ (violet circles) and P_{B0} (violet quadrangle) with F in water.

Figure 3(a) shows a typical evolution of $P_{\max}$ with respect to t, starting from a t of 20 ns. The $P_{\max}$ reaches 117 MPa at t = 20 ns and then decreases rapidly to 17 MPa at t = 100 ns; and afterwards, the pressure further decreases gradually to 1.5 MPa at t = 800 ns. It is evident that the pressure within the bubble, shown in Fig. 3(b), is significantly smaller. When t = 20 ns, 100 ns, and 800 ns, the P_B is only 0.177 MPa, 0.117 MPa and 0.104 MPa, respectively. A schematic of the cavitation bubble and the surrounding liquid is shown in Fig. 3(c). The low-pressure bubble is surrounded by a high-pressure fluid lamina. The fluid pressure just outside the bubble is equal to the liquid pressure far from the bubble as indicated in Eq. (5). Then the fluid pressure increases rapidly with increasing radius and reaches to the maximum at a radius of $4^{1/3}R$. Afterwards, the fluid pressure decreases gradually to the ambient liquid pressure.

The bulk modulus of water is ~2.2 GPa [24], which corresponds to a 5.3% change in volume for an external pressure change of 117 MPa. Consequently, the incompressibility assumption is valid here. Further verification of the fluid pressure changes under different values of F provides the same conclusion as well. In the following arguments, we will use $P_{\max}$ and P_B at a t = 20

Optics EXPRESS

ns to represent the initial $P_{max}(P_{max\,0})$ and initial $P_B(P_{B0})$. Figure 3(d) shows changes of $P_{max\,0}$ and P_{B0} with F in water. As the increase of F, P_{B0} reveals very limited changes, stable around 175-180 kPa. However, $P_{max\,0}$ increases with the increase of F, and an approximate empirical relationship $P_{max\,0} = 21F^{0.4}$ (MPa) can be obtained.

Focusing again on Eq. (1), when the bubble evolution with time can be written as a form of Eq. (1), an underlying conclusion is that the kinetic energy of the fluid during the bubble expansion is constant, i.e., the kinetic energy of the fluid is completely acquired during the incipient stage (t< 20 ns), which can be written as:

$$\int_R^\infty \rho\pi r^2 u^2 dr = 4\pi\rho a^4/25. \tag{10}$$

This conclusion is consistent with the results of Eq. (5). As $P(R) = P_\infty$, the expanding bubble does not provide additional mechanical work to the fluid. The duration of laser pulses (FWHM) used for ablation in our study is 20 ns, which means that at a t of 20 ns, only approximate half of the laser pulse energy has been input. Therefore, the above conclusion also indicates that when the bubble has grown to a certain size, the subsequent laser energy input would not affect the bubble dynamics obviously.

Combining the form of Eq. (1) and the results in Fig. 3(a), we can further conclude that the early fluid motion outside the cavitation bubbles is a spherical self-similar motion and can be described by an intense point explosion model proposed by L. I. Sedov [25]. This model has been widely used to describe the shockwaves generated during laser ablation of solid targets in air [26,27] and can also be used to describe the fluid motion during a strong underwater explosion [25,28]. For an incompressible liquid, when the pressure behind a fluid motion is so high that the counterpressure can be ignored, the governing parameters of the motion are the released energy during the explosion that drives the motion of fluid (E_0) and the liquid density. Thus, the radius of the expanding bubbles can also be rewritten as:

$$R = b(E_0/\rho)^{1/5} t^{2/5}, \tag{11}$$

where b is a dimensionless constant. Assuming that the released energy E_0 is totally converted into the kinetic energy of fluid, we get $b = (25/4\pi)^{1/5}$. This assumption is rational as the thermal conductivity of vapor is very small. Only a small amount of released energy can be converted into the internal energy of the surrounding fluid. The calculated E_0, represented by the energy conversion efficiency E_0/E (E is the laser pulse energy) is shown in Fig. 3(d). The E_0/E increases from 5.9% to 11.1% when F increases from 8.3 J/cm^2 to 46.4 J/cm^2 and then fluctuates slightly until F reaches of 90.6 J/cm^2. Further increase of F to 112.7 J/cm^2 results in a slight decrease of the conversion efficiency to 10.7%. As shown in Fig. 2(b), when using high F, some bubble contents could penetrate into the liquid after the formation of cavitation bubbles, which is a congruous reason for the decrease of E_0/E under high F.

Furthermore, we observed the early evolution of laser-induced cavitation bubbles in other common liquids, e.g., ethanol, n-butanol, and PEG200. We confirmed that the early evolution of laser-induced cavitation bubbles in these liquids can also be described by Eq. (1). Figure 4(a) and (b) show the evolution of shockwaves and cavitation bubbles in ethanol and the results are summarized in Fig. 4(c) and (d). An initial acceleration of the shockwaves is observed, and after ~40 ns, the speed of the shockwaves reaches a constant value, as shown in Fig. 4(c). Similar with that in water, the average shockwave speed in the first 300 ns increases slightly from 1286 m/s to 1355 m/s when the F increases from 29.8 J/cm^2 to 112.7 J/cm^2. By comparison, the sound speed in ethanol at 20 °C is 1160 m/s [29]. Figure 4(d) shows the evolution of cavitation bubbles in ethanol for three characteristic values of F. Cavitation bubbles expand faster in ethanol than in water. Comparisons between E_0, $P_{max\,0}$ and P_{B0} in water and ethanol are summarized in Table 1. The calculated E_0/E and P_{B0} in ethanol is higher than in water, but on the other hand, the calculated $P_{max\,0}$ in ethanol is lower than in water.

Optics EXPRESS

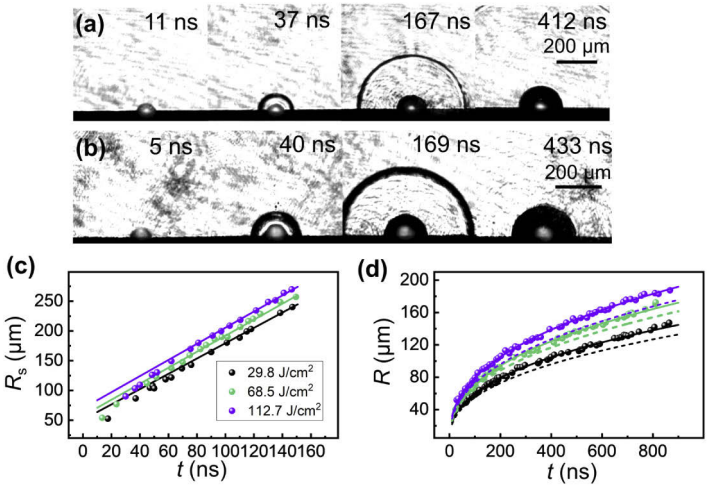

Fig. 4. (a, b) Shadowgraph images of shockwaves and cavitation bubbles generated after laser incidences in ethanol. F: (a) 29.8 J/cm^2 and (b) 112.7 J/cm^2. (c, d) Changes of R_s and R with t in ethanol. Solid lines in (c) and (d) are fitted curves by linear regression and Eq. (1), respectively. Dotted lines in (d): fitting curves in water under the corresponding F.

Table 1. Summary of calculated results in water and ethanol.

Liquid	F (J/cm^2)	E_0/E (%)	$P_{\max 0}$ (MPa)	P_{B0} (kPa)
Water	29.8	9.7	79.9	177.2
	68.5	11.0	117.0	176.3
	112.7	10.7	138.3	176.0
Ethanol	29.8	11.5	74.2	186.2
	68.5	11.9	105.1	186.0
	112.7	12.4	130.5	185.8

The results in four liquids under a typical F are further compared in Fig. 5, and Table 2 summarizes the properties of these liquids and the calculated results based on the early evolution of shockwaves and cavitation bubbles. Even though the surface tension and viscosity of these liquids differ greatly, the evolution of shockwaves and cavitation bubbles only changes slightly. The velocity of emitted shockwaves is similar to the sound speed in the corresponding liquid, which mainly depends on the bulk modulus and density of the liquid. Moreover, evolution of the generated cavitation bubbles is governed by the liquid density but not the surface tension nor viscosity of liquids. As the increase of liquid density, the generated cavitation bubbles expand slower. Nevertheless, the pressure within the bubble and in the surrounding fluid are affected by the surface tension and viscosity of liquids. Due to the high viscosity of *n*-butanol and PEG200, the bubble pressure in the two liquids is much higher than in other liquids. Factors affecting the released energy during the laser ablation (E_0/E) are more complicated. Various parameters, e.g., light absorption, latent heat of vaporization, may affect this value. Consequently, it does not simply depend on the listed liquid properties.

It is noteworthy that all the experimental results and discussions in our work focus on the bubble evolution after a t of 20 ns when the bubble has fully formed and grown to a distinguished size ($R > 25$ μm). The transient status of the laser-irradiated areas just after the laser incidence, the genesis and the earliest evolution of the bubble are still puzzles. It is well known that the conventional cavitation phenomena originate from the rapid changes of pressure in a liquid which

Optics EXPRESS

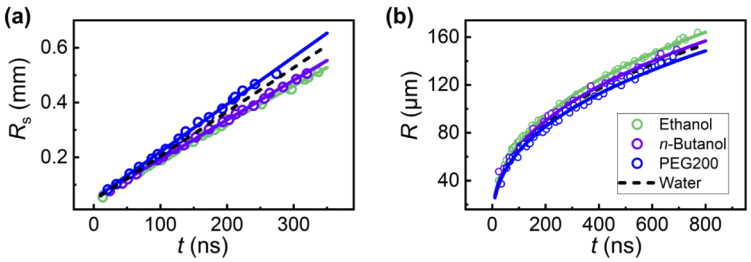

Fig. 5. Changes of (a) R_s and (b) R with t in water, ethanol, n-butanol and PEG200. F:68.5 J/cm^2. Solid lines (a) and (b) are fitted curves by linear regression and Eq. (1), respectively. Black dotted lines are fitting curves in water under the corresponding F.

Table 2. Summary of the liquid properties [30] and the calculated results based on the observed shockwaves and cavitation bubbles. *s* represents the average propagation speed of emitted shockwaves within the initial 300 ns. *F*: 68.5 J/cm^2.

Liquid	σ (mN/m)	μ (mPa · s)	ρ (kg/m^3)	s (m/s)	P_{B0} (kPa)	P_{max0} (MPa)	E_0/E (%)
Ethanol	22.4	1.05	789	1344	186.0	105.1	11.9
n-Butanol	24.7	2.54	815	1443	305.6	99.1	9.7
Water	72.5	0.89	998	1613	176.3	116.9	11.0
PEG200	43.5	63.8	1124	1732	5200.0	122.5	10.3

lead to the formation of small vapor-filled cavities. The pressure in these cavities is relatively low [17]. We believe that the formation of cavitation bubbles during laser ablation of submerged targets follows similar mechanisms. After the laser incidence, the absorbed laser energy results in the formation of a hot spot which enables the materials removal of the target surface and the evaporation of localized liquid, forming the nascent plasmas and vapor and emitting the shockwaves. The transient localized temperature and pressure can be extremely high. Afterward, the nascent plasmas and vapor further propel the rapid expansion of surrounding liquid, which enables the subsequent formation of discernible cavitation bubbles. From this perspective, the absorbed laser energy is partly transmitted to the surrounding fluid via the laser-induced plasmas and vapor at the very beginning and the subsequent expansion of cavitation bubble is a result of the motion of surrounding fluid. The E_0 represents this part of energy. Furthermore, as the rapid expansion of cavitation bubbles, the localized pressure drops sharply but the temperature may remain very high. This mechanism explains why the bubble is a low-pressure region that is bounded by a high-pressure fluid lamina when 20 ns $< t <$ 900 ns.

4. Conclusions

In summary, we presented a comprehensive analysis of the early cavitation bubble dynamics during laser ablation of titanium targets in liquids by employing high temporal resolution shadowgraph images. The early fluid displacement outside the cavitation bubble is a hemi-spherical self-similar motion. Consequently, the bubble radius can be fitted by a simple $t^{2/5}$ relationship, which enables analytic solutions of the pressure distribution within the bubble and in the surrounding liquid. The results show that the low-pressure bubble is surrounded by a high-pressure fluid lamina when $t >$ 20 ns, and its evolution is governed by the liquid density. The laser-induced cavitation bubbles expand slower in high density liquid. Other liquid properties do not affect the early bubble evolution significantly but the pressure within the bubble increases considerably in high viscosity liquids.

Optics EXPRESS

Funding

National Key R & D Program of China (2018YFB1107700); National Natural Science Foundation of China (51805093, 51775117, 51575114); Natural Science Foundation of Guangdong Province (2018A030310578); Science and Technology Planning Project of Guangdong Province (2017B090911013); Chinese Scholars Council.

Acknowledgments

The work was conducted at the Laser Thermal Laboratory. The authors are thankful to Prof. Stephen Morris from Mechanical Engineering of UC Berkeley for the kind discussion about the fluid mechanics.

Disclosures

The authors declare no conflicts of interest.

References

1. A. H. Clauer, "Laser shock peening, the path to production," Metals **9**(6), 626 (2019).
2. V. M. Tabie, M. O. Koranteng, A. Yunus, and F. Kuuyine, "Water-Jet Guided Laser Cutting Technology- an Overview," Lasers Manuf. Mater. Process. **6**(2), 189–203 (2019).
3. Q. Zheng, Z. Fan, G. Jiang, A. Pan, Z. Yan, Q. Lin, J. Cui, W. Wang, and X. Mei, "Mechanism and morphology control of underwater femtosecond laser microgrooving of silicon carbide ceramics," Opt. Express **27**(19), 26264 (2019).
4. H. Zeng, X.-W. Du, S. C. Singh, S. A. Kulinich, S. Yang, J. He, and W. Cai, "Nanomaterials via Laser Ablation/Irradiation in Liquid: A Review," Adv. Funct. Mater. **22**(7), 1333–1353 (2012).
5. V. Amendola and M. Meneghetti, "Laser ablation synthesis in solution and size manipulation of noble metal nanoparticles," Phys. Chem. Chem. Phys. **11**(20), 3805–3821 (2009).
6. S. Ibrahimkutty, P. Wagener, A. Menzel, A. Plech, and S. Barcikowski, "Nanoparticle formation in a cavitation bubble after pulsed laser ablation in liquid studied with high time resolution small angle x-ray scattering," Appl. Phys. Lett. **101**(10), 103104 (2012).
7. P. Wagener, S. Ibrahimkutty, A. Menzel, A. Plech, and S. Barcikowski, "Dynamics of silver nanoparticle formation and agglomeration inside the cavitation bubble after pulsed laser ablation in liquid," Phys. Chem. Chem. Phys. **15**(9), 3068–3074 (2013).
8. B. Kumar, D. Yadav, and R. K. Thareja, "Growth dynamics of nanoparticles in laser produced plasma in liquid ambient," J. Appl. Phys. **110**(7), 074903 (2011).
9. K. Liu, J. Chen, H. Qu, Y. Dong, Y. Gao, J. Liu, X. Liu, Y. Zou, and H. Zeng, "Bubble dimer dynamics induced by dual laser beam ablation in liquid," Appl. Phys. Lett. **113**(2), 021902 (2018).
10. J. Lam, J. Lombard, C. Dujardin, G. Ledoux, S. Merabia, and D. Amans, "Dynamical study of bubble expansion following laser ablation in liquids," Appl. Phys. Lett. **108**(7), 074104 (2016).
11. K. Sasaki and N. Takada, "Liquid-phase laser ablation," Pure Appl. Chem. **82**(6), 1317–1327 (2010).
12. T. Tsuji, Y. Okazaki, Y. Tsuboi, and M. Tsuji, "Nanosecond Time-Resolved Observations of Laser Ablation of Silver in Water," Jpn. J. Appl. Phys. **46**(4A), 1533–1535 (2007).
13. H. Hu, T. Liu, and H. Zhai, "Comparison of femtosecond laser ablation of aluminum in water and in air by time-resolved optical diagnosis," Opt. Express **23**(2), 628 (2015).
14. A. Kanitz, D. J. Förster, J. S. Hoppius, R. Weber, A. Ostendorf, and E. L. Gurevich, "Pump-probe microscopy of femtosecond laser ablation in air and liquids," Appl. Surf. Sci. **475**, 204–210 (2019).
15. T. T. P. Nguyen, R. Tanabe-Yamagishi, and Y. Ito, "Impact of liquid layer thickness on the dynamics of nano- to sub-microsecond phenomena of nanosecond pulsed laser ablation in liquid," Appl. Surf. Sci. **470**, 250–258 (2019).
16. Rayleigh Lord, "On the pressure developed in a liquid during the collapse of a spherical cavity," Philos. Mag. **34**(200), 94–98 (1917).
17. C. E. Brennen, *Cavitation and Bubble Dynamics* (Cambridge University, 2013).
18. R. Löfstedt, B. P. Barber, and S. J. Putterman, "Toward a hydrodynamic theory of sonoluminescence," Phys. Fluids A **5**(11), 2911–2928 (1993).
19. W. Soliman, T. Nakano, N. Takada, and K. Sasaki, "Modification of Rayleigh-Plesset theory for reproducing dynamics of cavitation bubbles in liquid-phase laser ablation," Jpn. J. Appl. Phys. **49**(11), 116202 (2010).
20. A. De Giacomo, M. Dell'Aglio, A. Santagata, R. Gaudiuso, O. De Pascale, P. Wagener, G. C. Messina, G. Compagnini, and S. Barcikowski, "Cavitation dynamics of laser ablation of bulk and wire-shaped metals in water during nanoparticles production," Phys. Chem. Chem. Phys. **15**(9), 3083–3092 (2013).
21. N. Walsh, J. T. Costello, and T. J. Kelly, "Optical diagnostics of laser-produced aluminium plasmas under water," Appl. Phys. B: Lasers Opt. **123**(6), 179 (2017).

Optics EXPRESS

22. A. Tamura, A. Matsumoto, K. Fukami, N. Nishi, and T. Sakka, "Simultaneous observation of nascent plasma and bubble induced by laser ablation in water with various pulse durations," J. Appl. Phys. **117**(17), 173304 (2015).
23. M. Greenspan and C. E. Tschiegg, "Speed of Sound in Water by a Direct Method," J. Res. Natl. Bur. Stan. **59**(4), 249–254 (1957).
24. Y. A. Cengel and J. M. Cimbala, *Fluid Mechanics: Fundamentals and Applications* (McGraw-Hill Higher Education, 2006).
25. L. I. Sedov, *Similarity and Dimensional Analysis in Mechanics*, 10 Edition (CRC, 1993).
26. C. Porneala and D. A. Willis, "Time-resolved dynamics of nanosecond laser-induced phase explosion," J. Phys. D: Appl. Phys. **42**(15), 155503 (2009).
27. N. Zhang, X. Zhu, J. Yang, X. Wang, and M. Wang, "Time-resolved shadowgraphs of material ejection in intense femtosecond laser ablation of aluminum," Phys. Rev. Lett. **99**(16), 167602 (2007).
28. V. K. Kedrinskii, *Hydrodrnamics of explosions: experiments and models* (Springer, 2005).
29. R. Wegge, M. Richter, and R. Span, "Speed of sound measurements in ethanol and benzene over the temperature range from (253.2 to 353.2) K at pressures up to 30 MPa," J. Chem. Eng. Data **60**(5), 1345–1353 (2015).
30. D. R. Lide, *CRC Handbook of Chemistry and Physics*, 85th Edition (CRC, 2004).

114.70.5.203 2020-04-30 19:03:14